Status of the INL high-temperature electrolysis research programme – experimental and modelling

J.E. O'Brien,[1] **J.S. Herring,**[1] **C.M. Stoots,**[1] **M.G. McKellar,**[1]
E.A. Harvego,[1] **K.G. Condie,**[1] **G.K. Housley,**[1] **J.J. Hartvigsen**[2]
[1]Idaho National Laboratory, Idaho Falls, ID USA
[2]Ceramatec, Inc., Salt Lake City, UT USA

Abstract

This paper provides a status update on the high-temperature electrolysis (HTE) research and development programme at Idaho National Laboratory (INL), with an overview of recent large-scale system modelling results and the status of the experimental programme. System analysis results have been obtained using the commercial code UniSim, augmented with a custom high-temperature electrolyser module. The process flow diagrams for the system simulations include an advanced nuclear reactor as a source of high-temperature process heat, a power cycle and a coupled steam electrolysis loop. Several reactor types and power cycles have been considered, over a range of reactor coolant outlet temperatures.

In terms of experimental research, the INL has recently completed an Integrated Laboratory Scale (ILS) HTE test at the 15 kW level. The initial hydrogen production rate for the ILS test was in excess of 5 000 litres per hour. Details of the ILS design and operation will be presented. Current small-scale experimental research is focused on improving the degradation characteristics of the electrolysis cells and stacks. Small-scale testing ranges from single cells to multiple-cell stacks. The INL is currently in the process of testing several state-of-the-art anode-supported cells and is working to broaden its relationship with industry in order to improve the long-term performance of the cells.

Introduction

High-temperature nuclear reactors have the potential for substantially increasing the efficiency of hydrogen production from water, with no consumption of fossil fuels, no production of greenhouse gases, and no other forms of air pollution. Water-splitting for hydrogen production can be accomplished via high-temperature electrolysis (HTE) or thermochemical processes, using high-temperature nuclear process heat. In order to achieve competitive efficiencies, both processes require high-temperature operation (~850°C). Thus these hydrogen-production technologies are tied to the development of advanced high-temperature nuclear reactors. High-temperature electrolytic water-splitting supported by nuclear process heat and electricity has the potential to produce hydrogen with overall thermal-to-hydrogen efficiencies of 50% or higher, based on high heating value. This efficiency is near that of the thermochemical processes (Yildiz, 2006; O'Brien, 2008a, 2008b), but without the severe corrosive conditions of the thermochemical processes and without the fossil fuel consumption and greenhouse gas emissions associated with hydrocarbon processes.

A research programme is under way at the Idaho National Laboratory (INL) to simultaneously address the technical and scale-up issues associated with the implementation of solid-oxide electrolysis cell technology for efficient hydrogen production from steam. We are co-ordinating a progression of electrolysis cell and stack testing activities, at increasing scales, along with a continuation of supporting research activities in the areas of materials development, single-cell testing, detailed computational fluid dynamics (CFD) analysis and system modelling.

The INL HTE programme also includes an investigation of the feasibility of producing syngas by simultaneous electrolytic reduction of steam and carbon dioxide (co-electrolysis) at high temperature using solid-oxide cells. Syngas, a mixture of hydrogen and carbon monoxide, can be used for the production of synthetic liquid fuels via Fischer-Tropsch processes. This concept, coupled with nuclear energy, provides a possible path toward reduced greenhouse gas emissions and increased energy independence, without the major infrastructure shift that would be required for a purely hydrogen-based transportation system (O'Brien, 2009; Stoots, 2009; Jensen, 2007; Mogensen, 2008). Furthermore, if the carbon dioxide feedstock is obtained from biomass, the entire concept would be carbon-neutral.

HTE plant process models

A number of detailed process models have been developed for large-scale system analysis of high-temperature electrolysis plants. These analyses have been performed using UniSim process analysis software (Honeywell, 2005). UniSim is a derivative of HYSYS. The software inherently ensures mass and energy balances across all components and includes thermodynamic data for all chemical species. The overall process includes a very high-temperature helium-cooled reactor (VHTR) coupled to the direct helium recuperated Brayton power cycle and an HTE plant with air sweep (O'Brien, 2008a). The reactor thermal power assumed for the high-temperature helium-cooled reactor is 600 MW_{th}. For the base case, the primary helium coolant exits the reactor at 900°C. This helium flow is split, with more than 90% of the flow directed toward the power cycle and the remainder directed to the intermediate heat exchanger to provide process heat to the HTE loop. Within the power-cycle loop, helium flows through the power turbine where the gas is expanded to produce electric power. The helium, at a reduced pressure and temperature, then passes through a recuperator and pre-cooler where it is further cooled before entering the low-pressure compressor. To improve compression efficiencies, the helium is again cooled in an intercooler heat exchanger before entering the high-pressure compressor. The helium exits the high-pressure compressor at a pressure that is slightly higher than the reactor operating pressure of 7 MPa. The coolant then circulates back through the recuperator where the recovered heat raises its temperature to the reactor inlet temperature of 647°C, completing the cycle.

The HTE process is operated at elevated pressure (3.5 MPa) for two reasons. Elevated pressure supports higher mass flow rates for the same size components. Furthermore, the gaseous hydrogen product will ultimately be delivered at elevated pressure either for storage or pipeline. Therefore, from the standpoint of overall process efficiency, it is logical to compress the liquid water feedstock at the process inlet since liquid-phase compression work is very small compared to compression of the gaseous product. Heat recuperation is used in the process to the maximum extent possible in order to minimise the net process heat requirement. A fraction of the product gas is recycled and mixed with the inlet steam in order to assure that reducing conditions are maintained on the steam/hydrogen

electrode. The process gas mixture is heated to the electrolysis operating temperature in the intermediate heat exchanger (IHX), using high-temperature process heat from the nuclear reactor. The process stream then enters the electrolyser, where the steam is electrolytically reduced, yielding hydrogen on the cathode side of each cell and oxygen on the anode side. Most of the components included in the analysis are standard UniSim components. However, a custom electrolyser module was developed at INL for direct incorporation into the UniSim system analysis code, as described in detail in O'Brien (2005).

The baseline process uses air as a sweep gas, to remove the excess oxygen that is evolved on the anode side of the electrolyser. For the air-sweep cases, inlet air is compressed to the system operating pressure of 3.5 MPa in a four-stage compressor with intercooling. The final compression stage is not followed by a cooler, so the air enters the IHX at about 120°C. The sweep gas is heated to the electrolyser operating temperature of 800°C via the IHX which supplies high-temperature nuclear process heat directly to the system. The sweep gas then enters the electrolyser, where it is combined with product oxygen. Finally, it passes through the electrolysis recuperator to help preheat the incoming process gas. Some of the sweep gas compression work is recovered using a sweep-gas turbine located at the sweep-gas exit. In order to avoid the work requirement associated with compression of the sweep gas, it is possible to operate with no sweep gas, and to allow the system to produce pure oxygen, which could potentially be supplied to another collocated process such as an oxygen-blown gasifier. For this mode of operation, the four-stage air compressor would not be included in the process flow diagram and there would be no air flow through the intermediate heat exchanger. Air preheat at the IHX is no longer needed. Oxygen would simply be evolved from the anode side of the electrolyser at the electrolysis operating pressure and temperature. It would flow through the electrolysis heat recuperator and the outlet turbine. The results of our system analyses have shown that this concept is desirable from the standpoint of overall process efficiency, but there are significant technical issues associated with handling high-temperature pure oxygen that would have to be addressed. Similar system analyses have been performed to evaluate the concept of direct syngas production from steam and carbon dioxide using HTE.

For these simulations, the per-cell active area for electrolysis was assumed to be 225 cm^2. This cell size is well within the limits of current technology for planar cells. A temperature-dependent area-specific resistance (ASR) was used to characterise the performance of the electrolysis cells (Stoots, 2005). In order to show the trends that can be expected with higher or lower ASR, two values of ASR_{1100K} have been included in this study. The ASR_{1100K} value of 1.25 represents a stack-average *ASR* value at 1 100 K that is achievable in the short term with existing technology. The ASR_{1100K} value of 0.25 is an optimistic value that has been observed in button cells, but will be difficult to achieve in a stack in the short term. The temperature dependence of the *ASR* is important for the adiabatic cases (since the outlet temperature in these cases is generally different than the inlet temperature) and for evaluating the effect of electrolyser inlet temperature on overall process efficiency.

The total number of cells used in the process simulations was determined by specifying a maximum current density for each ASR value considered that was large enough to ensure that the operating voltage would just exceed the thermal neutral voltage. For the higher nominal ASR value of 1.25 Ohm·cm^2, the maximum current density was set at 0.25 A/cm^2 and an adiabatic thermal boundary condition was assumed. The total number of cells for this base case was adjusted until the total remaining power was zero. In other words, the full power cycle output at this operating point is dedicated to electrolysis. This procedure resulted in 1.615×10^6 cells required. At lower current densities, the power cycle output exceeds the value required for electrolysis and this excess power would be supplied to the grid. For the case of ASR = 0.25 Ohm·cm^2, the maximum current density was set at 1.0 A/cm^2. A much higher maximum current density was required for the lower *ASR* case, again in order to assure that the thermal neutral voltage was just exceeded.

Two thermal boundary condition limits were considered for the electrolyser: isothermal and adiabatic. Actual electrolyser operation will generally lie between these limits. For the isothermal cases, heat from the reactor was directly supplied to the electrolyser to maintain isothermal conditions for operation below the thermal neutral voltage. Heat rejection from the electrolyser is required to maintain isothermal operation at operating voltages above thermal neutral. For the adiabatic cases, the direct electrolyser heater was not used.

To allow for performance comparisons between HTE and alternate hydrogen production techniques, we have adopted a general overall efficiency definition that can be applied to any thermal

water-splitting process, including HTE, low-temperature electrolysis (LTE), and thermochemical processes. Since the primary energy input to all of these processes is ultimately in the form of heat, the appropriate general efficiency definition to be applied to all of the techniques is the overall thermal-to-hydrogen efficiency, η_H. This efficiency is defined as the heating value of the produced hydrogen divided by the total thermal input required to produce it. In this report, the lower heating value (LHV) of the produced hydrogen has been used:

$$\eta_H = \frac{LVH}{\sum_i Q_i} \tag{1}$$

The denominator in this efficiency definition quantifies all of the net thermal energy that is consumed in the process, either directly or indirectly. For a thermochemical process, the majority of the high-temperature heat from the reactor is supplied directly to the process as heat. For HTE, the majority of the high-temperature heat is supplied directly to the power cycle and indirectly to the HTE process as electrical work. Therefore, the summation in the denominator of Eq. (1) includes the direct nuclear process heat as well as the thermal equivalent of any electrically driven components such as pumps, compressors, HTE units, etc. The thermal equivalent of any electrical power consumed in the process is the power divided by the thermal efficiency of the power cycle. For an electrolysis process, the summation in the denominator of Eq. (1) includes the thermal equivalent of the primary electrical energy input to the electrolyser and the secondary contributions from smaller components such as pumps and compressors. In additional, any direct thermal inputs are also included. Direct thermal inputs include any net (not recuperated) heat required to heat the process streams up to the electrolyser operating temperature and any direct heating of the electrolyser itself required for isothermal operation.

System analysis results

A summary of results obtained from the hydrogen production system analyses is presented in Figures 1 and 2. The results presented in these figures were obtained for a fixed steam utilisation of 89%. In order to maintain fixed steam utilisation, the flow rates of the process streams were adjusted with lower flow rates for lower current densities and higher flow rates for higher current densities. The results of eight cases are presented in Figure 1: low and high ASR, adiabatic and isothermal electrolyser operation, air-sweep and no-sweep. The figure provides overall hydrogen production efficiencies [Eq. (1)] as a function of per-cell operating voltage. Recall that electrolyser efficiency is inversely proportional to operating voltage (O'Brien, 2008b). Higher operating voltages yield higher current densities and higher hydrogen production rates, but lower overall efficiencies, so the selection of electrolyser operating condition is a trade-off between production rate and efficiency. For a specified

Figure 1: Overall HTE hydrogen production efficiencies for the VHTR/recuperated direct Brayton cycle, as a function of per-cell operating voltage

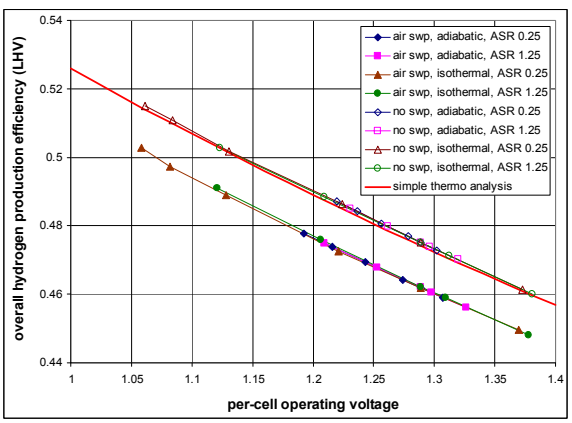

Figure 2: (a) Overall hydrogen production efficiency as a function of hydrogen production rate, with air sweep; (b) effect of steam utilisation on overall hydrogen production efficiency

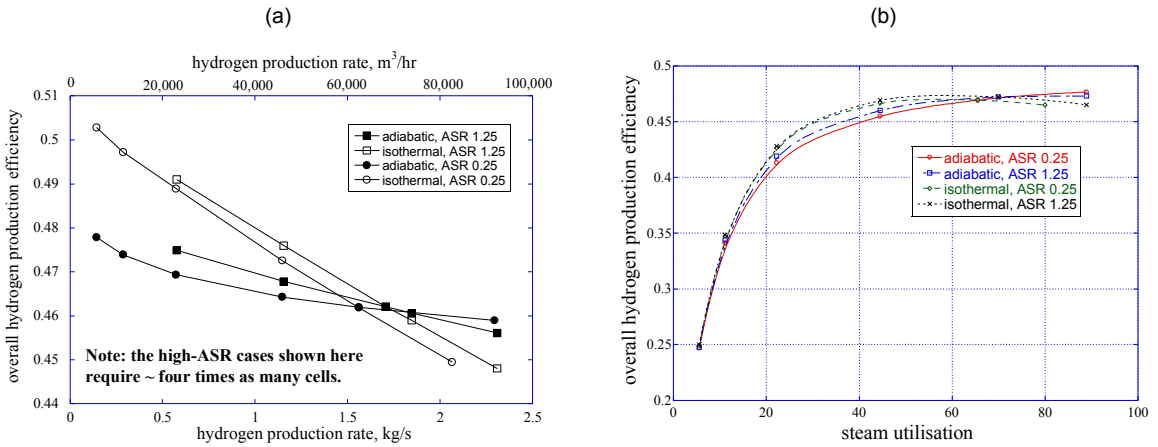

target production rate, higher production efficiency requires a higher capital cost, since more cells would be required to achieve the target production rate. In general, a good trade-off between production rate and efficiency occurs for operating voltages near or slightly below the thermal neutral value, around 1.29 V. This operating voltage is also desirable from the standpoint that the electrolysis stack operates nearly isothermally at this voltage. Predicted overall thermal-to-hydrogen efficiency values shown in Figure 1 are generally within 8 percentage points of the power-cycle efficiency of 52.6%, decreasing with operating voltage. It is interesting to note that the overall process efficiencies for these fixed-utilisation cases collapse onto individual lines, one for the air-sweep cases and another for the no-sweep cases, when plotted as a function of per-cell operating voltage, regardless of the electrolyser mode of operation (adiabatic or isothermal) and ASR value. Note that the highest operating voltages shown are just above the thermal neutral voltage of 1.29 V. Note also that the highest overall efficiency plotted in Figure 1 (for no-sweep, ASR = 0.25, isothermal, V = 1.06 A/cm^2) exceeds 51%.

An additional line, based on a simple thermodynamic analysis (O'Brien 2008b) is also shown in Figure 1. This analysis considers a control volume drawn around the electrolysis process, with the process consuming the electrical work from the power cycle, and heat from a high-temperature source. If the inlet and outlet streams are assumed to be liquid water, and gaseous hydrogen and oxygen, respectively, at $T = T^o$, $P = P^o$, direct application of the first law, Faraday's law, and the definition of the overall thermal-to-hydrogen efficiency yields:

$$\eta_H = \frac{LHV}{2FV_{op}(1/\eta_{th} - 1) + HHV} \tag{2}$$

The curve labelled "simple thermo analysis" in Figure 1 represents Eq. (2). This equation provides a useful reference against which detailed system analyses can be measured. The simple thermodynamic analysis agrees quite closely with the detailed system analysis results for the no-sweep cases, which correspond directly with the conditions of simple analysis since it does not include consideration of a sweep gas. Overall hydrogen efficiency results of the air-sweep cases are about 1% lower than the no-sweep cases.

Hydrogen production efficiencies can also be plotted as a function of hydrogen production rate, as shown in Figure 2(a). As expected, efficiencies decrease with production rate since higher production rates require higher current densities and higher per-cell operating voltages, for a fixed number of cells. For this plot, the full 600 MW_{th} output of the reactor is assumed to be dedicated to hydrogen production. Under this assumption about four times as many electrolysis cells are required for the high-ASR cases than for the low-ASR cases, with a correspondingly higher associated capital cost. Figure 2(a) shows that hydrogen production rates in excess of 2.3 kg/s (92 000 SCMH, 78×10^6 SCF/day) could be achieved with a dedicated 600 MW_{th} hydrogen-production plant. This rate is the same order of magnitude as a large hydrogen production plant based on steam-methane reforming. Figure 2(a) indicates similar overall efficiencies for the low-ASR and high-ASR cases at a specified electrolyser thermal operating condition (adiabatic or isothermal) and hydrogen production rate.

The effect of steam utilisation was examined by fixing the electrolyser inlet process gas flow rates at the values that yielded 89% utilisation at the current density associated with the thermal neutral voltage for each ASR value, then varying the current density over the range of values considered for the fixed-utilisation cases. Low current densities for this case yield low values of steam utilisation since the inlet steam flow rate is fixed. Results of this exercise are presented in Figure 2(b). The overall efficiency results for the variable-utilisation cases nearly collapse onto a single curve when plotted versus utilisation. The plot indicates a strong dependence on utilisation, with overall hydrogen production efficiencies less than 25% at the lowest utilisation values shown (~5.5%), increasing to a maximum value of ~47% at the highest utilisation value considered (89%). So, from the overall system perspective, low steam utilisation is bad. This is an interesting result because, from the perspective of the electrolyser alone, low utilisation yields high electrolyser (not overall) efficiency values. Excess steam in the electrolyser keeps the average Nernst potential low for each cell, which assures a low operating voltage for a specified current density (or hydrogen production rate). However, from the overall system perspective, low steam utilisation means that the system is processing lots of excess material, resulting in relatively high irreversibilities associated with incomplete heat recuperation, pumping and compression of excess process streams, etc. Above ~50% utilisation, however, the efficiency curves are relatively flat, even decreasing slightly for the isothermal cases. Regarding very high utilisation values, achievement of steam utilisation values much above 90% is not practical from an operational standpoint because localised steam starvation can occur on the cells, with associated severe performance penalties and possible accelerated cell lifetime degradation.

The effect of reactor outlet temperature has also been considered. Figure 3 shows overall hydrogen production efficiencies, based on high heating value in this case, plotted as a function of reactor outlet temperature. The figure includes a curve that represents 65% of the thermodynamic maximum possible efficiency for any thermal water-splitting process, assuming heat addition occurs at the reactor outlet temperature and heat rejection occurs at T_L = 20°C (O'Brien, 2008b). In order to cover a broad range of possible reactor outlet temperatures, three different advanced-reactor/power-conversion combinations were considered: a helium-cooled reactor coupled to a direct recuperative Brayton cycle, a supercritical CO_2-cooled reactor coupled to a direct recompression cycle, and a sodium-cooled fast reactor coupled to a Rankine cycle. Each reactor/power-conversion combination was analysed over an appropriate reactor outlet temperature range.

Figure 3: Overall thermal-to-hydrogen efficiencies for HTE coupled to three different reactor types, as a function of reactor outlet temperature

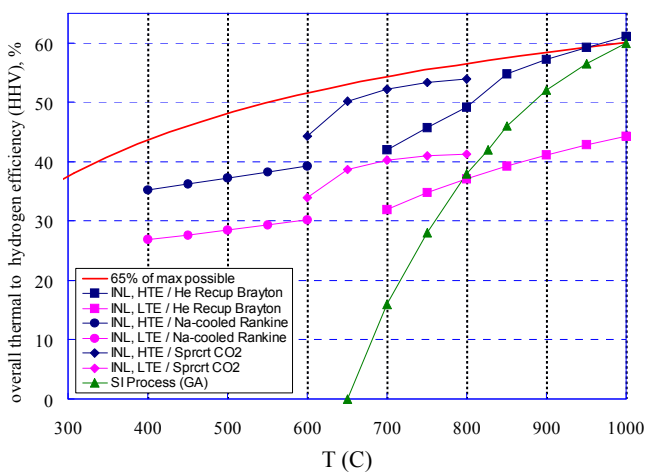

The figure shows results for both HTE and low-temperature electrolysis (LTE). In addition, an efficiency curve for the SI thermochemical process is shown (Brown, 2003). The results presented in Figure 3 indicate that, even when detailed process models are considered, with realistic component efficiencies, heat exchanger performance, and operating conditions, overall hydrogen production efficiencies in excess of 50% can be achieved for HTE with reactor outlet temperatures above 850°C. For reactor outlet temperatures in the range of 600-800°C, the supercritical CO_2/recompression power

cycle is superior to the He-cooled/Brayton cycle concept. This conclusion is consistent with results presented by Yildiz (2006). The efficiency curve for the SI process also includes values above 50% for reactor outlet temperatures above 900°C, but it drops off quickly with decreasing temperature, and falls below values for LTE coupled to high-temperature reactors for outlet temperatures below 800°C. Note that even LTE benefits from higher reactor outlet temperatures because of the improved power conversion thermal efficiencies. Current planning for NGNP (Southworth, 2003) indicates that reactor outlet temperatures will be at or below 850°C, which favours HTE.

Experimental programme

The experimental programme at INL includes a range of test activities designed to characterise the performance of solid-oxide cells operating in the electrolysis mode. Small-scale activities are intended to examine candidate electrolyte, electrode and interconnect materials with single cells and small stacks. Initial cell and stack performance and long-term degradation characteristics have been examined. Larger scale experiments are designed to demonstrate the technology and to address system-level issues such as hydrogen recycle and heat recuperation.

A photograph of the INL high-temperature electrolysis laboratory is shown in Figure 4. This part of the laboratory is dedicated to small-scale experiments with single cells and small stacks. The laboratory is currently being upgraded and will soon include three furnaces for single and button cell tests, plus two larger furnaces for stack testing. A schematic of the experimental apparatus used for single-cell testing is presented in Figure 5. The schematic for stack testing is similar. Primary components include gas supply cylinders, mass-flow controllers, a humidifier, on-line dew point and CO_2 measurement stations, temperature and pressure measurement, high-temperature furnace, a solid oxide electrolysis cell, and a gas chromatograph. Nitrogen is used as an inert carrier gas. Carbon dioxide and related instrumentation is included for co-electrolysis experiments. Inlet flow rates of nitrogen, hydrogen, carbon dioxide and air are established by means of precision mass-flow controllers. Hydrogen is included in the inlet flow as a reducing gas in order to prevent oxidation of the nickel cermet electrode material. Air flow to the stack is supplied by the shop air system, after passing through a two-stage extractor/dryer unit. The cathode-side inlet gas mixture, consisting of hydrogen, nitrogen, and possibly carbon dioxide (for co-electrolysis tests) is mixed with steam by means of a heated humidifier. The dew point temperature of the nitrogen/hydrogen/CO_2/steam gas mixture exiting the humidifier is monitored continuously using a precision dew point sensor. All gas lines located downstream of the humidifier are heat-traced in order to prevent steam condensation. Inlet and outlet CO_2 concentrations are also monitored continuously using on-line infrared CO_2 sensors, when applicable.

For single button-cell testing, an electrolysis cell is bonded to the bottom of a zirconia tube, using a glass seal. During testing, the tube is suspended in the furnace. The cells are electrolyte-supported with a scandia-stabilised zirconia electrolyte, about 150 μm thick. The outside electrode, which is exposed to air, acts as the cathode in fuel cell mode and the anode in electrolysis mode. This electrode is a doped manganite. The inside steam-hydrogen electrode (electrolysis cathode) material is a nickel cermet. Both button-cell electrodes incorporate a platinum wire mesh for current distribution and

Figure 4: High-temperature electrolysis laboratory at INL – small-scale experiments

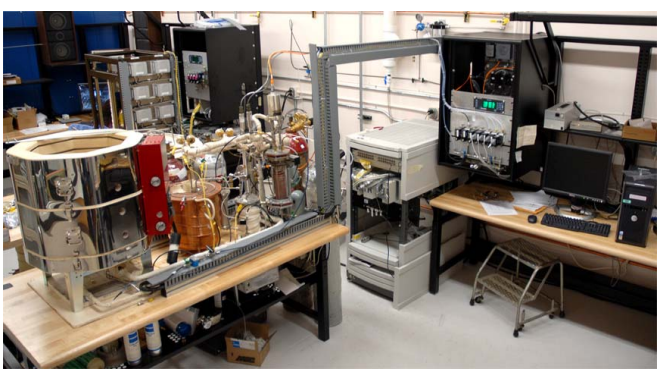

Figure 5: Schematic of single-cell co-electrolysis test apparatus

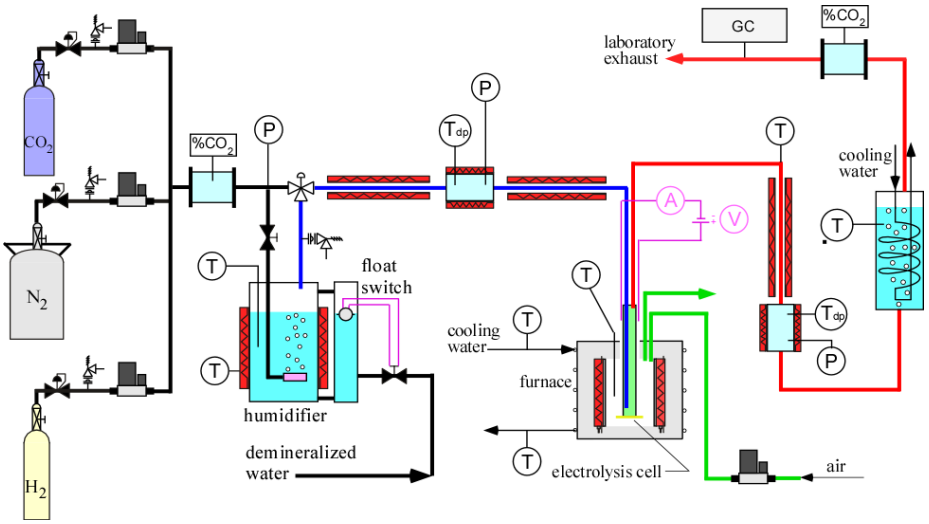

collection. The button cells include both an active cell area (2.5 cm^2 for the cell shown) and a reference cell area. The active cell area is wired with both power lead wires and voltage taps. The reference cell area is wired only with voltage taps, allowing for continuous monitoring of open-cell potential. The power lead and voltage wires are routed to the far end of the zirconia tube via several small-diameter alumina tubes fixed to the outside of the zirconia manifold tube. A type-K stainless-steel sheathed thermocouple is mounted on the manifold tube and bent around in front of the button cell in order to allow for continuous monitoring of the button-cell temperature. The inlet gas mixture enters this tube, directing the gas to the steam/hydrogen/CO_2 side (inside) of the cell. The cell is maintained at an appropriate operating temperature (800 to 850°C) via computer-based feedback control. The furnace also preheats the inlet gas mixture and the air sweep gas. Oxygen produced by electrolysis is captured by the sweep gas stream and expelled into the laboratory. The product stream exits the zirconia tube and is directed towards the downstream dew point and CO_2 sensors and then to a condenser through a heat-traced line. The condenser removes most of the residual steam from the exhaust. The final exhaust stream is vented outside the laboratory through the roof. Rates of steam and CO_2 electrolysis are monitored by the measured change in inlet and outlet steam and CO_2 concentration as measured by the on-line sensors. In addition, a gas chromatograph (GC) has been incorporated into the facility downstream of the condenser to precisely quantify the composition of the dry constituents in the electrolysis product stream (including any CH_4 that may be produced).

The majority of the stack testing that has been performed at INL to date has been with planar stacks fabricated by Ceramatec, Inc. of Salt Lake City, UT. An exploded view of the internal components of one of these stacks is shown in Figure 6. The cells have an active area of 64 cm^2. The stacks are designed to operate in cross flow, with the steam/hydrogen gas mixture flowing from front to back in the figure and air flowing from right to left. Air flow enters at the rear though an air inlet manifold and exits at the front directly into the furnace. The power lead attachment tabs, integral with the upper and lower interconnect plates, are also visible in Figure 6. Stack operating voltages were measured using wires that were directly spot-welded onto these tabs. The interconnect plates are fabricated from ferritic stainless steel. Each interconnect includes an impermeable separator plate (~0.46 mm thick) with edge rails and two corrugated "flow fields," one on the air side and one on the steam/hydrogen side. The height of the flow channel formed by the edge rails and flow fields is 1.0 mm. Each flow field includes 32 perforated flow channels across its width to provide uniform gas-flow distribution. The steam/hydrogen flow fields are fabricated from nickel foil. The air-side flow fields are ferritic stainless steel. The interconnect plates and flow fields also serve as electrical conductors and current distributors. To improve performance, the air-side separator plates and flow fields are pre-surface-treated to form a rare-earth stable conductive oxide scale. A perovskite rare-earth coating is also applied as a bond layer to the separator-plate oxide scale by either screen printing or plasma spraying. On the steam/hydrogen side of the separator plate, a thin (~10 μm) nickel metal coating is applied as a bond layer.

Figure 6: Exploded view of electrolysis stack components

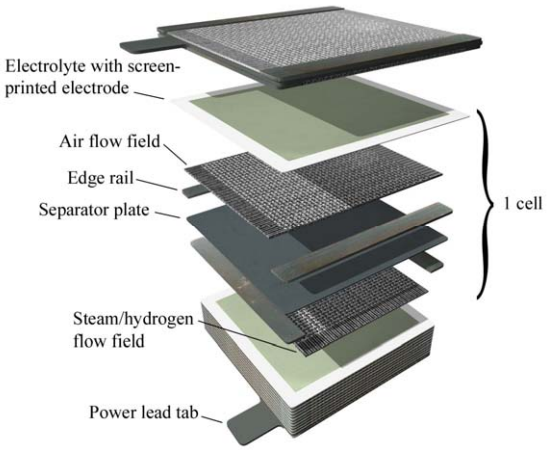

The stack electrolytes are scandia-stabilised zirconia, about 140 μm thick. The air-side electrodes (anode in the electrolysis mode) are a strontium-doped manganite. The electrodes are graded, with an inner layer of manganite/zirconia (~13 μm) immediately adjacent to the electrolyte, a middle layer of pure manganite (~18 μm), and an outer bond layer of cobaltite. The steam/hydrogen electrodes (cathode in the electrolysis mode) are also graded, with a nickel-zirconia cermet layer (~13 μm) immediately adjacent to the electrolyte and a pure nickel outer layer (~10 μm).

Results of initial single (button) cell HTE tests completed at the INL were documented in detail in O'Brien (2005). Button cell tests are useful for basic performance characterisation of electrode and electrolyte materials and of different cell designs (*e.g.* electrode-supported, integrated planar, tubular). Polarisation curves for several representative DC potential sweeps are presented in Figure 7(a). Both the applied cell potentials and the corresponding power densities are plotted in the figure as a function of cell current density. Positive current densities indicate fuel cell mode of operation and negative current densities indicate electrolysis mode. Cell potential values at zero current density correspond to open-circuit potentials, which depend on the furnace temperature and the gas composition. The three sweeps acquired at 800°C (sweeps 1, 3 and 5) have a steeper E-i slope, due to the lower zirconia ionic conductivity at the lower temperature. The continuous nature of the E-i curves across the zero-current density (open-circuit) point provides no indication of significant activation overpotential for these electrolyte-supported cells. In the electrolysis mode, the voltage data vary linearly with current density up to a value that depends on the inlet steam flow rate, which for a fixed dry-gas flow rate depends on the inlet dew point temperature. For low inlet dew point values (sweeps 1 and 2), the voltage begins to increase rapidly at relatively low values of current density (~ -0.15 A/cm^2), due to steam starvation. For higher inlet dew points, the steam starvation effect is forestalled to higher current densities. The single-cell results demonstrated the feasibility of HTE for hydrogen production linear operation from the fuel-cell to the electrolysis mode.

Results of initial short-stack HTE tests performed at INL are provided by O'Brien (2006, 2007). A good summary of our experience is provided by the results plotted in Figure 7(b), also from O'Brien (2007). Results of several representative sweeps are shown in the form of polarisation curves, representing per-cell operating voltage versus current density. Test conditions for each of the seven sweeps are tabulated in the figure. Five of the sweeps were obtained from a 10-cell stack (sweeps 10-1 through 10-5) and two were obtained from a 25-cell stack (25-1 and 25-2). Theoretical open-cell potential values are shown in the figure for each sweep using a single data point at zero current density. Note that the measured open-cell potentials are in excellent agreement with the theoretical values for each sweep. Sweep 10-1 was performed with a relatively low inlet steam flow rate, corresponding to the low inlet dew point value of 48.5°C and relatively low nitrogen and hydrogen flow rates. This sweep has a relatively high slope on i-V co-ordinates, indicating a relatively high ASR. This sweep also clearly shows the effects of steam starvation; the slope of the *i-V* curve increases dramatically as the current density is increased. The outlet dew point temperature corresponding to the highest current density shown in this figure was only 4°C for this sweep. Sweep 10-2 was performed

Figure 7: Polarisation curves

(a) Button cell

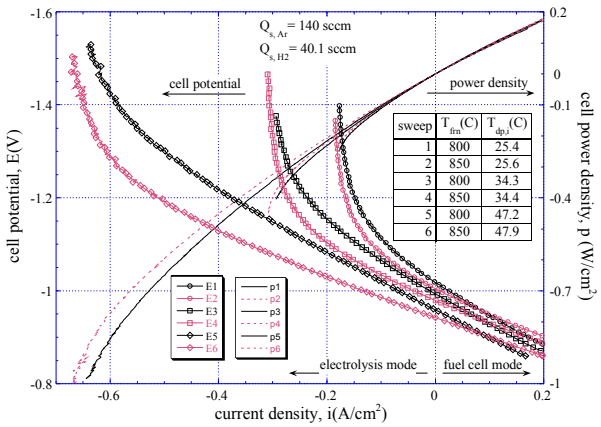

(b) Planar stack

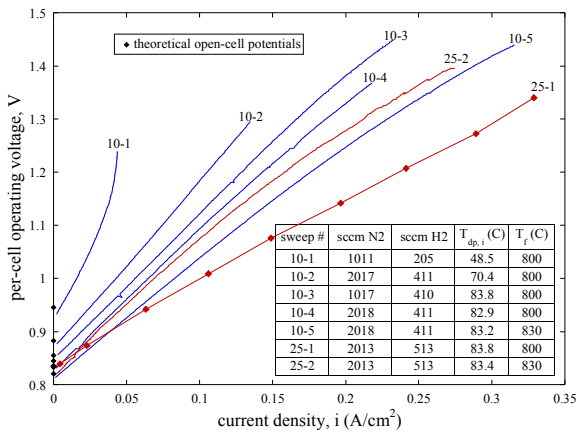

at an intermediate steam concentration, with an inlet dew point temperature of 70°C. This sweep exhibits nearly linear behaviour over the range of current densities shown, with a much smaller slope than sweep 10-1. Sweeps 10-3 and 10-4 are nearly linear at low current densities, then slightly concave-down at higher current densities. Sweep 10-5 has a shallower slope than the others, consistent with the higher operating temperature of 830°C. Sweep 25-1 was performed in a stepwise fashion, rather than as a continuous sweep. This was done in order to ensure sufficient time for the internal stack temperatures to achieve steady-state values at each operating voltage. Note that the slope of this sweep is small, indicating low *ASR* (~1.5 Ω·cm²). This sweep was performed at the beginning of a 1 000-hour long-duration 25-cell stack test. Sweep 25-2 was acquired at the end of the long-duration test. The stack operating temperature was increased from 800°C to 830°C partway through the test. Note that the slope of sweep 25-2 is higher than that of sweep 25-1, despite the higher temperature, due to performance degradation over 1 000 hours of operation.

Representative co-electrolysis results are presented in Figure 8 (Stoots, 2007). This figure shows the outlet gas composition (dry basis) from a ten-cell electrolysis stack as a function of stack current. The solid data symbols represent measurements obtained from the gas chromatograph. The lines represent predictions based on our chemical equilibrium co-electrolysis model (CECM) (O'Brien, 2007). The open data symbols show the cold inlet mole fractions of CO_2, H_2 and CO (zero). Note that these values are different than the zero-current outlet compositions shown in the figure. Even without any electrolysis, the reverse-shift reaction occurs in the stack at 800°C, resulting in the production of some CO and consumption of CO_2 and H_2. During co-electrolysis, the mole fractions of CO_2 and steam (not shown in Figure 8) decrease with current, while the mole fractions of H_2 and CO increase. For the conditions chosen for these tests, the ratio of H_2 to CO is close to the desired 2-to-1 value for syngas production.

The issue of long-term performance degradation is critical if the potential of large-scale hydrogen production based on HTE is ever to be realised. Performance degradation is also an important issue for solid-oxide fuel cells (SOFC) and addressing this issue has been a major focus of both the US DOE SECA programme (Williams, 2006) and the European Real-SOFC programme (Steinberger, 2007). Significant progress has been made in identifying and mitigating degradation mechanisms in SOFC. But the electrolysis mode of operation presents some unique possible degradation mechanisms that have received much less attention. Observations of long-term performance degradation of solid-oxide electrolysis cells have been documented at INL. It should be noted that most of the cells and stacks tested at INL utilise scandia-stablised zirconia (ScSZ) electrolyte-supported cells which do not necessarily represent the state-of-the-art in cell design. Furthermore, the scandia dopant level in these cells was only about 6 mol%, which is not high enough to be considered fully stabilised. In addition, ScSZ with dopant levels less than 10% have been shown to exhibit an ageing effect with annealing at 1 000°C (Haering, 2005).

Figure 8: Outlet gas composition as a function of current density for co-electrolysis experiments, 10-cell stack

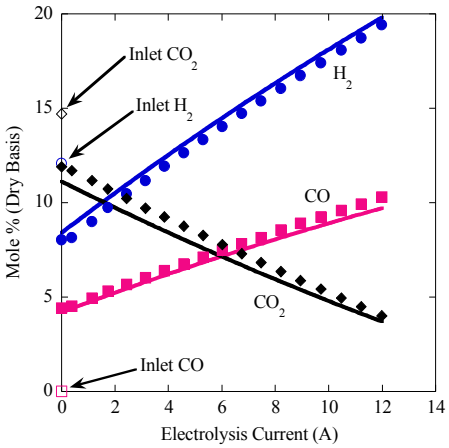

Long-term degradation in button cell tests can only be due to degradation of the electrodes, the electrolyte, or electrode-electrolyte delamination. There are no effects associated with corrosion, contact resistance, flow fields, or interconnects, since these components are not present. Results of one long-term button-cell test are presented in Figure 9(a). This figure shows the area-specific resistance (ASR) of a button cell plotted as a function of time over the duration of an 1 100-hour test. The ASR increases relatively rapidly at the start of the test from an initial value of ~0.6 Ohm cm^2 to a value of 0.9 Ohm cm^2 over about 40 hours. Between 100 hours and 1 100 hours, the ASR increases from 0.98 Ohm cm^2 to 1.33 Ohm cm^2. If the initial 100 hours is considered to be a cell conditioning period, the degradation rate over the following 1 000 hours is about 35%. This is obviously an unacceptable rate of degradation. As a comparison, the Phase-III SECA target degradation rate is 0.1%/1 000 hr. Several companies are currently coming very close to meeting that target in the SOFC mode of operation.

Figure 9: (a) Area-specific resistance of a button cell as a function of time for 1 100-hour test; (b) area-specific resistance of a 25-cell stack as a function of time for a 1 000-hour test

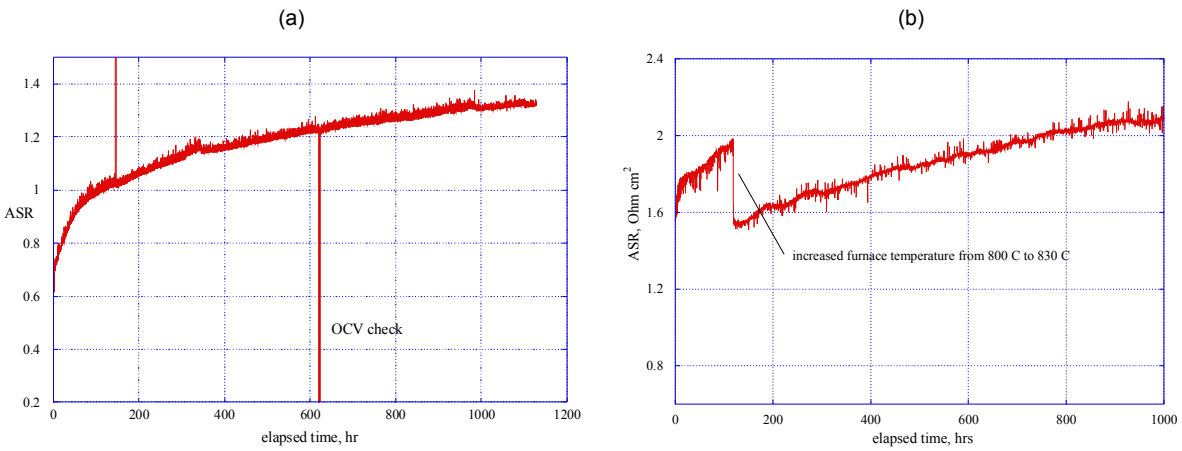

Performance degradation results with an SOEC stack tested at INL were also presented in O'Brien (2007). Results of a 1 000-hour test performed with a 25-cell stack are presented in Figure 9(b). This figure provides a plot of the stack area-specific resistance as a function of time for the 1 000 hours. The furnace temperature was increased from 800 to 830°C over an elapsed time of 118 hours, resulting in a sudden drop in ASR. The increase in ASR with time represents a degradation in stack performance. The degradation rate decreases with time and is relatively low for the last 200 hours of the test. However, from the 118-hour mark to the end of the test, ASR increased more than 40% over roughly 900 hours. Reduction of this performance degradation is an objective of ongoing research.

One of the objectives of the INL HTE programme is technology scale-up and demonstration. To this end, the INL has developed a 15 kW HTE test facility, termed the Integrated Laboratory Scale (ILS) HTE test facility. Details of the design and initial operation of this facility are documented in Housley (2007) and Stoots (2008, 2009). A condensed description of the facility will be provided here. The ILS includes three electrolysis modules, each consisting of four stacks of 60 cells, yielding 240 cells per module and 720 cells total. The cells are similar to those discussed earlier. Each electrolysis module utilises an independent support system supplying electrical power for electrolysis, a feedstock gas mixture of hydrogen and steam (and sometimes nitrogen), a sweep gas, and appropriate exhaust handling. Each module includes a controlled inlet flow of deionised water, a steam generator, a controlled inlet flow of hydrogen, a superheater, inlet and outlet dew point measurement stations, a condenser for residual steam, and a hydrogen vent. All three modules were located within a single hot zone. Heat recuperation and hydrogen product recycle were also incorporated into the facility. A photograph of the ILS is provided in Figure 10.

Figure 10: INL 15 kW Integrated Laboratory Scale HTE test facility

An exploded view of one of the ILS module assemblies including the recuperative heat exchanger, base manifold unit, and four-stack electrolysis unit is presented in Figure 11. For each four-stack electrolysis module, there were two heat exchangers and one base manifold unit. Each base manifold unit has nine flow tubes entering or exiting at its top and only four flow tubes entering or exiting at the bottom of the unit and at the bottom of the heat exchangers, thereby reducing the number of tube penetrations passing through the hot zone base plate from nine to just four. This feature also reduces the thermal load on the hot zone base plate. An internally manifolded plate-fin design concept was selected for this heat recuperator application. This design provides excellent configuration flexibility in terms of selecting the number of flow elements per pass and the total number of passes in order to satisfy the heat transfer and pressure drop requirements. Theoretical counterflow heat exchanger performance can be approached with this design. This design can also accommodate multiple fluids in a single unit. More details of the design of the recuperative heat exchangers are provided in Housley (2008).

Figure 12 shows a rendering of the three ILS electrolysis modules with their base manifolds and heat exchangers beneath. This illustration also shows the instrumentation wires for intermediate voltage and temperature readings. Each module is instrumented with twelve 1/16” sheathed thermocouples for monitoring gas temperatures in the electrolysis module manifolds and in the base manifold. These thermocouples are attached to the manifolds using compression fittings. There are also 12 miniature 0.020” diameter inconel-sheathed type-K thermocouples per module that are used for monitoring internal stack temperatures. Access to the internal region of the stacks is provided via the air outlet face. The internal thermocouples are inserted into the small exit air flow channels. Similarly, seven intermediate voltage tap wires per module are inserted into the air flow channels of the four stacks.

Figure 11: Exploded view of heat exchanger, base manifold unit, and four-stack electrolysis unit

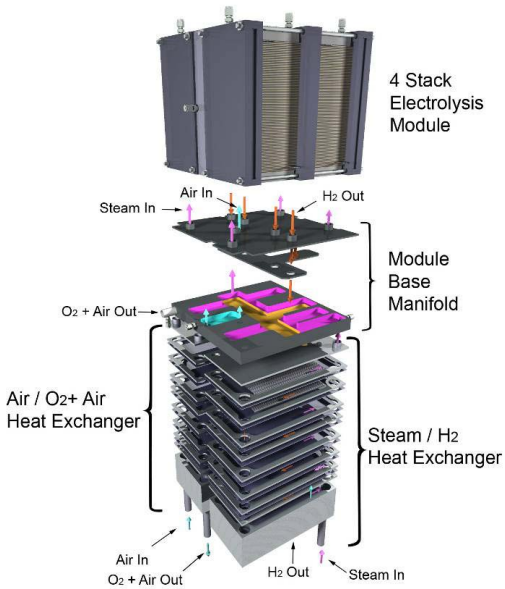

Figure 12: ILS modules, mounted in hot zone

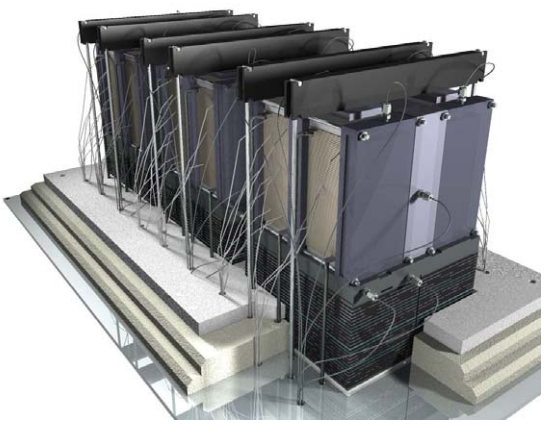

Two compression bars are shown across the top of each module in Figure 12. These bars are used to maintain compression on all of the stacks during operation in order to minimise electrical contact resistance between the cells, flow fields and interconnects. The bars are held in compression via spring-loaded tie-downs located outside of the hot zone under the base plate.

Note that the heat exchangers are partially imbedded in the insulation thickness. The top portion of each heat exchanger is exposed to the hot zone radiant environment, which helps to insure that the inlet gas streams achieve the desired electrolyser operating temperature prior to entering the stacks. The temperature at the bottom of each heat exchanger will be close to the inlet stream temperature, minimising the thermal load on the hot zone base plate in the vicinity of the tubing penetrations.

Performance degradation with the ILS system is documented in Figure 13. Over a period of 700 hours of test time, module-average ASR values increased by about a factor of 5, from an initial value near 1.5 Ohm·cm^2. Some of the observed degradation was related to balance-of-plant issues. For example, prior to about 480 hours of operation, unanticipated condensation occurred in the hydrogen recycle system which led to erratic control of the hydrogen recycle flow rate due to the intermittent presence of liquid water in the mass flow controllers. This problem led to time periods during which there may have been no hydrogen flow to the ILS stacks, leading to accelerated performance degradation

Figure 13: ILS hydrogen production rate time history

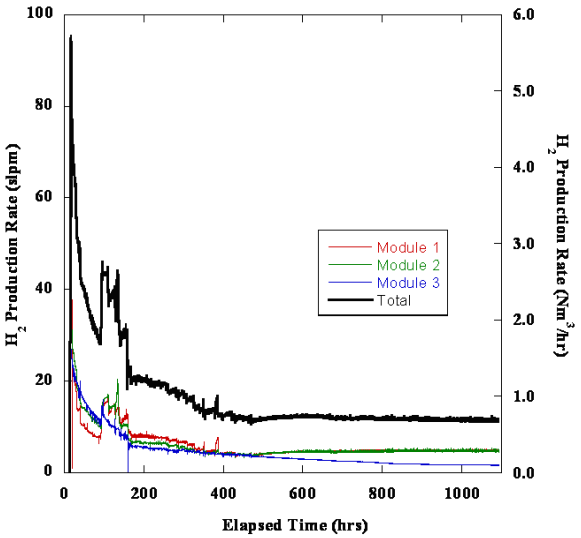

associated with oxidation of the nickel cermet electrodes. Despite the problems with the ILS, we were able to successfully demonstrate large-scale hydrogen production. A plot of the time history of ILS hydrogen production is given in Figure 13. Peak electrolysis power consumption and hydrogen production rate were 18 kW and 5.7 Nm^3/hr, respectively, achieved at about 17 hours of elapsed test time.

Single-cell tests – anode-supported cells

INL is currently in the process of testing several state-of-the-art single 5 cm × 5 cm anode-supported cells in the electrolysis mode. A new test apparatus has been developed for this purpose. Referring to the exploded view given in Figure 14, the steam hydrogen mixture enters through the inlet hole in the bottom of the HastX base plate. It then flows through a diverging flow channel milled into the HastX base plate and passes through a slot in the bottom of the alumina cell holder. The steam/hydrogen then flows under the cell through a corrugated/perforated nickel flow field. A nickel foil underneath the flow field will serve as a current collector. A power lead and voltage tap double-ended wire will be spot welded to the nickel foil and will be situated in one of the grooves of the flow field. These wires will be fed out through holes in the bottom of the alumina cell holder. There will also be a nickel mesh (not shown) in direct contact with the anode above the flow field. A nickel paste will be used to enhance electrical contact between the cell and the nickel mesh, flow field and foil. The steam/hydrogen flow exits through a slot in the cell holder and then through a converging flow channel cut into the base plate and out through the steam/H2 outlet hole in the base plate.

Air is introduced to the cathode side of the cell through holes in the HastX top plate and the alumina air flow distributor. The air flow inlet tube will be welded to the HastX top plate and will protrude into the hole in the alumina air flow distributor. A seal will be formed between the HastX top plate and the alumina air flow distributor by means of a mica gasket or ceramic paste. After exiting the air flow distributor, the air will impinge on the air side of the cell and flow radially outward through an array of protuberances milled into the bottom side of the alumina air flow distributor plate. The air then exits into the furnace volume. A platinum or silver mesh is situated between the air flow distributor and the cathode. A platinum or silver ink will be used to enhance electrical contact between the air electrode and the mesh. A power lead/voltage tap double-ended wire will be spot-welded to the current collector mesh and will be situated in one of the grooves formed by the array of protuberances. It can then be fed out of the fixture from the side.

A fixed compressive load is applied to the entire cell stack-up between the alumina cell holder and the HastX top plate by means of weights, as shown in the test stand overview, Figure 15. This load must simultaneously compress the cell against the mesh, flow field and foil on the steam/hydrogen side and against the seal around the outer edge of the cell. The outer edge of the cell rests on a window

Figure 14: Exploded view of single cell fixture

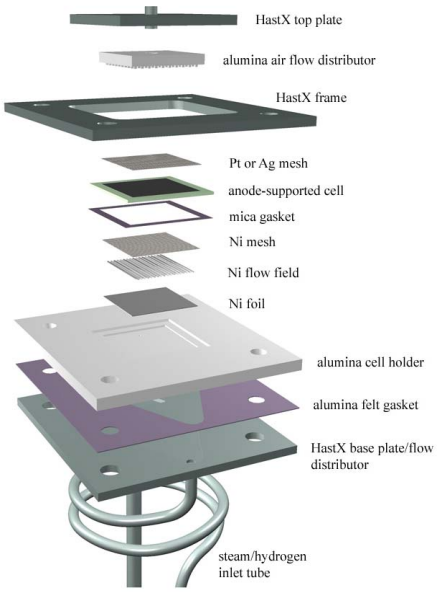

Figure 15: Single-cell test stand overview

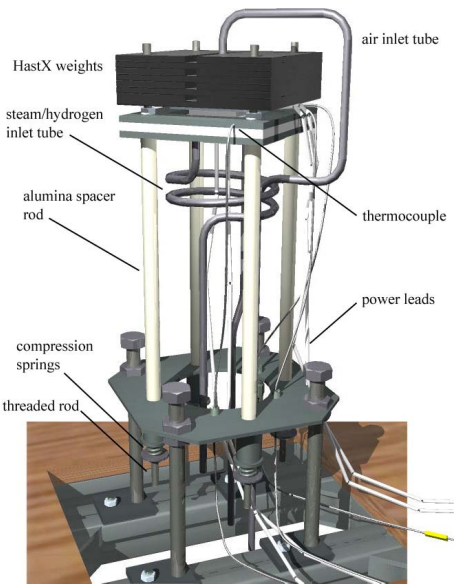

frame shelf milled into the alumina cell holder. The seal will be accomplished using a high-temperature SOFC sealing paste. The weight plates are held in alignment by the upper portion of the threaded rods which extend upward for this purpose. There are eight weight plates, each 1.2 lbs, for a total of 9.6 lbs, which yields a compressive pressure of about 20 000 Pa on the cell active area.

A fixed compressive load is independently applied between the HastX frame, the alumina cell holder, and the HastX base plate. This load is generated by the compression of four springs located under the test stand base support outside of the furnace. The springs will be compressed a fixed amount that is determined by the height of the spool pieces. This load is intended to compress the seal between the cell holder and the base plate. This seal will be formed by either a mica gasket or a ceramic sealing paste. A nut is visible on the threaded rod in Figure 15 just above the HastX frame and

below the weight plates. This nut represents the upper stop for this compressive load. The extension of the threaded rods above the nuts is for the purpose of aligning the weight plates. Note that the weight plates are floating above these nuts since they are resting on the HastX top plate.

The air and steam/hydrogen flow tubes will be fabricated from inconel. HastX was specified for the base plate, the frame and the weight plates. The spacer rods are specified as alumina in order to minimise heat conduction out of the bottom of the furnace.

Conclusions

An overview of the high-temperature electrolysis research and development programme at the Idaho National Laboratory has been presented, with selected observations of electrolysis cell degradation at the single-cell, small stack and large (15 kW) facility scales. Large-scale system analyses performed at the INL have demonstrated the potential for high-temperature electrolysis as a large-scale hydrogen production technology. Successful operation of the 15 kW integrated laboratory scale facility for over 1 000 hours was completed in the fall of 2008. However, several issues require further research, including cell and stack long-term performance degradation. Degradation has been identified as a major issue that must be solved for high-temperature electrolysis to ultimately achieve any significant level of deployment.

Acknowledgements

This work was supported by the US Department of Energy, Office of Nuclear Energy, Nuclear Hydrogen Initiative and Next Generation Nuclear Plant Programs under DOE Operations Office Contract DE-AC07-05ID14517.

References

Brown, L.C., R.D. Lentsch, G.E. Besenbruch, K.R. Schultz (2003), "Alternative Flowsheets for the Sulfur-Iodine Thermochemical Hydrogen Cycle", *AIChE Journal,* April.

Haering, C., A. Roosen, H. Schichl, M. Schnoller (2005), "Degradation of the Electrical Conductivity in Stabilized Zirconia System Part II: Scandia-stabilised Zirconia", *Solid Sate Ionics*, Vol. 176, No. 3-4, pp. 261-268, January.

Honeywell International Inc., UniSim Design, R360 Build 12073, Copyright ©2005-2006.

Housley, G., K. Condie, J.E. O'Brien, C.M. Stoots (2007), "Design of an Integrated Laboratory Scale Experiment for Hydrogen Production via High Temperature Electrolysis", *ANS Embedded Topical: International Topical Meeting on the Safety and Technology of Nuclear Hydrogen Production, Control, and Management*, 24-28 June, Boston, Massachusetts, USA, paper no. 172431.

Housley, G.K., J.E. O'Brien, G.L. Hawkes (2008), "Design of a Compact Heat Exchanger for Heat Recuperation from a High Temperature Electrolysis System", *2008 ASME International Congress and Exposition*, Boston, MA, USA, November, paper# IMECE2008-68917.

Mogensen, M., S.H. Jensen, A. Hauch, I. Chorkendorff, T. Jacobsen (2008), "Reversible Solid Oxide Cells", *Ceramic Engineering and Science Proceedings*, Vol. 28, No. 4, *Advances in Solid Oxide Fuel Cells III* – A Collection of Papers Presented at the 31st International Conference on Advanced Ceramics and Composites, pp. 91-101.

O'Brien, J.E., C.M. Stoots, J.S. Herring, P.A. Lessing, J.J. Hartvigsen, S. Elangovan (2005), "Performance Measurements of Solid-oxide Electrolysis Cells for Hydrogen Production", *Journal of Fuel Cell Science and Technology*, Vol. 2, pp. 156-163, August.

O'Brien, J.E., C.M. Stoots, J.S. Herring, J.J. Hartvigsen (2006), "Hydrogen Production Performance of a 10-cell Planar Solid-oxide Electrolysis Stack", *Journal of Fuel Cell Science and Technology*, Vol. 3, pp. 213-219, May.

O'Brien, J.E., C.M. Stoots, J.S. Herring, J.J. Hartvigsen (2007), "Performance of Planar High-temperature Electrolysis Stacks for Hydrogen Production from Nuclear Energy", *Nuclear Technology*, Vol. 158, pp. 118-131, May.

O'Brien, J.E., M.G. McKellar, J.S. Herring (2008a), "Performance Predictions for Commercial-scale High-temperature Electrolysis Plants Coupled to Three Advanced Reactor Types", *2008 International Congress on Advances in Nuclear Power Plants*, Anaheim, CA, 8-12 June.

O'Brien, J.E. (2008b), "Thermodynamic Considerations for Thermal Water Splitting Processes and High-temperature Electrolysis", 2008 ASME International Congress and Exposition, Boston, MA, USA, November, paper# IMECE2008-68880.

O'Brien, J.E., M.G. McKellar, C.M. Stoots, J.S. Herring, G.L. Hawkes (2009), "Parametric Study of Large-scale Production of Syngas via High Temperature Electrolysis", *International Journal of Hydrogen Energy*, forthcoming.

Southworth, F., P.E. Macdonald, D.J. Harrell, C.V. Park, E.L. Shaber, M.R. Holbrook, D.A. Petti (2003), "The Next Generation Nuclear Plant (NGNP) Project", *Proceedings GLOBAL 2003*, pp. 276-287.

Steinberger-Wilkens, R., F. Tietz, M.J. Smith, J. Mougin, B. Rietveld, O. Bucheli, J. Van Herle, Z. Mohsine, P. Holtappels (2007), "Real-SOFC – A Joint European Effort in Understanding SOFC Degradation", *ECS Transactions*, Vol. 7, No. 1, *Part 1, ECS Transactions – 10th International Symposium on Solid Oxide Fuel Cells, SOFC-X*, pp. 67-76.

Stoots, C.M., J.E. O'Brien, M.G. McKellar, G.L. Hawkes, J.S. Herring (2005), "Engineering Process Model for High-temperature Steam Electrolysis System Performance Evaluation", *AIChE 2005 Annual Meeting*, Cincinnati, OH, USA, 30 October-4 November.

Stoots, C.M., J.E. O'Brien (2008), "Initial Operation of the High-temperature Electrolysis Integrated Laboratory Scale Experiment at INL", *2008 International Congress on Advances in Nuclear Power Plants*, Anaheim, CA, USA, 8-12 June.

Stoots, C.M., J.E. O'Brien (2009), "Results of Recent High-temperature Co-electrolysis Studies at the Idaho National Laboratory", *International Journal of Hydrogen Energy*, forthcoming.

Stoots, C.M., J.E. O'Brien, K. Condie, L. Moore-McAteer, G.K. Housley, J.J. Hartvigsen, J.S. Herring (2009), "The High-temperature Electrolysis Integrated Laboratory Experiment", *Nuclear Technology*, April.

Williams, M.C., J.P. Strakey, W.A. Surdoval, L.C. Wilson (2006), "Solid Oxide Fuel Cell Technology Development in the US", *Solid State Ionics*, Vol. 177, No. 19-25, pp. 2039-2044, October.

Yildiz, B., M.S. Kazimi (2006), "Efficiency of Hydrogen Production Systems Using Alternative Nuclear Energy Technologies", *Int. J. of Hydrogen Energy*, Vol. 31, pp. 77-92.

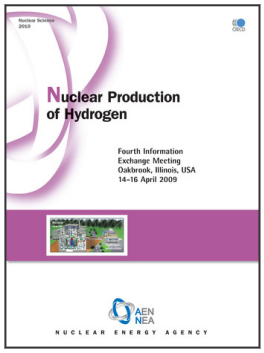

From:

Nuclear Production of Hydrogen

Fourth Information Exchange Meeting, Oakbrook, Illinois, USA , 14-16 April 2009

Access the complete publication at:

https://doi.org/10.1787/9789264087156-en

Please cite this chapter as:

O'Brien, James E.*, et al.* (2010), "Status of the INL high-temperature electrolysis research programme – experimental and modelling", in OECD, *Nuclear Production of Hydrogen: Fourth Information Exchange Meeting, Oakbrook, Illinois, USA , 14-16 April 2009*, OECD Publishing, Paris.

DOI: https://doi.org/10.1787/9789264087156-11-en

This work is published under the responsibility of the Secretary-General of the OECD. The opinions expressed and arguments employed herein do not necessarily reflect the official views of OECD member countries.

This document and any map included herein are without prejudice to the status of or sovereignty over any territory, to the delimitation of international frontiers and boundaries and to the name of any territory, city or area.

You can copy, download or print OECD content for your own use, and you can include excerpts from OECD publications, databases and multimedia products in your own documents, presentations, blogs, websites and teaching materials, provided that suitable acknowledgment of OECD as source and copyright owner is given. All requests for public or commercial use and translation rights should be submitted to rights@oecd.org. Requests for permission to photocopy portions of this material for public or commercial use shall be addressed directly to the Copyright Clearance Center (CCC) at info@copyright.com or the Centre français d'exploitation du droit de copie (CFC) at contact@cfcopies.com.